Soil Moisture Sensing with UAV-Mounted IR-UWB Radar and Deep Learning

RONG DING, HAIMING JIN*, DONG XIANG, XIAOCHENG WANG, YONGKUI ZHANG, and DINGMAN SHEN, Shanghai Jiao Tong University, China
LU SU, Purdue University, USA
WENTIAN HAO and MINGYUAN TAO, Damo Academy, Alibaba Group, China
XINBING WANG, Shanghai Jiao Tong University, China
CHENGHU ZHOU, Chinese Academy of Sciences, China

Wide-area soil moisture sensing is a key element for smart irrigation systems. However, existing soil moisture sensing methods usually fail to achieve both satisfactory mobility and high moisture estimation accuracy. In this paper, we present the design and implementation of a novel soil moisture sensing system, named as SoilId, that combines a UAV and a COTS IR-UWB radar for wide-area soil moisture sensing without the need of burying any battery-powered in-ground device. Specifically, we design a series of novel methods to help SoilId extract soil moisture related features from the received radar signals, and automatically detect and discard the data contaminated by the UAV's uncontrollable motion and the multipath interference. Furthermore, we leverage the powerful representation ability of deep neural networks and carefully design a neural network model to accurately map the extracted radar signal features to soil moisture estimations. We have extensively evaluated SoilId against a variety of real-world factors, including the UAV's uncontrollable motion, the multipath interference, soil surface coverages, and many others. Specifically, the experimental results carried out by our UAV-based system validate that SoilId can push the accuracy limits of RF-based soil moisture sensing techniques to a 50% quantile MAE of 0.23%.

CCS Concepts: • **Human-centered computing → Ubiquitous and mobile computing**.

Additional Key Words and Phrases: Soil Moisture Sensing; UAV; IR-UWB Radar; Deep Learning.

ACM Reference Format:
Rong Ding, Haiming Jin, Dong Xiang, Xiaocheng Wang, Yongkui Zhang, Dingman Shen, Lu Su, Wentian Hao, Mingyuan Tao, Xinbing Wang, and Chenghu Zhou. 2023. Soil Moisture Sensing with UAV-Mounted IR-UWB Radar and Deep Learning. *Proc. ACM Interact. Mob. Wearable Ubiquitous Technol.* 7, 1, Article 11 (March 2023), 25 pages. https://doi.org/10.1145/3580867

1 INTRODUCTION

Timely, accurate, and wide-area soil moisture sensing plays an important role in smart irrigation for agriculture. First, it helps to preserve the irrigational water usage. Reportedly, more than 15% of the earth's fresh water is wasted due to overwatering in agriculture [1]. Such wastage of the invaluable fresh water resource could be

*Corresponding author.

Authors' addresses: Rong Ding; Haiming Jin; Dong Xiang; Xiaocheng Wang; Yongkui Zhang; Dingman Shen, Shanghai Jiao Tong University, China, {dingrong,jinhaiming,xx627460225cy,curryjam_cg,zykk-2333,631322231}@sjtu.edu.cn; Lu Su, Purdue University, USA, lusu@purdue.edu; Wentian Hao; Mingyuan Tao, Damo Academy, Alibaba Group, China, {wentian.hwt,mingyuan.tmy}@alibaba-inc.com; Xinbing Wang, Shanghai Jiao Tong University, China, xwang8@sjtu.edu.cn; Chenghu Zhou, Chinese Academy of Sciences, China, zhouch@lreis.ac.cn.

2474-9567/2023/3-ART11 $15.00
https://doi.org/10.1145/3580867

greatly alleviated, if we could sense when the soil contains enough water, and refrain irrigation accordingly [2]. Besides, the crops grow optimally only when they are irrigated properly at the right time and amount. Thus, accurate soil moisture sensing in real time enables smart irrigation systems to dynamically optimize the irrigation schedule to meet the requirements of the specific types of the grown crops, which eventually helps improve crop yields [3]. Apart from agricultural applications, soil moisture sensing also brings crucial benefits to other real-world tasks, such as eco-environment monitoring [4], outdoor sports field (e.g., golf court, football field) maintenance [5], and many others.

Thus far, a series of techniques have been proposed for soil moisture sensing, which can be categorized into the sensor-based and RF-based ones. Specifically, the operation mode of the sensor-based techniques are to bury dedicated sensor nodes in the soil, such as electricity resistance sensors [6, 7], tensiometers sensors [8], and radioactive sensors [9]. However, such techniques typically have the following limitations. First, the sensor-based techniques have to rely on various types of peripherals, such as data loggers and communication modules, to store and transmit the collected sensory data. Installing and connecting these devices into the whole moisture sensing system usually require professional knowledge and much effort. Second, a typical farm oftentimes needs tens or even hundreds of moisture sensors to provide enough sensing coverage. Clearly, the maintenance operations, including battery change and faulted device replacement, of an in-ground sensor network with such scale are rather prohibitive.

Unlike the sensor-based techniques, the RF-based ones employ the RF signals to estimate the soil moisture without installing the aforementioned dedicated sensors in the soil. However, existing RF-based techniques have their own limitations, as well. Some of them require to bury battery-powered devices in the soil, such as Wi-Fi receivers [10], LoRa nodes [11, 12], and radar backscatter tags [13], which thus suffer from the risk of soil contamination from battery corruption, as well as the excessive labor works for battery change. In contrast, a variety of other RF-based techniques do not depend on any battery-powered in-ground devices. Among them, the remote sensing approaches [14–17] use radars attached on satellites or planes for soil moisture estimation through the RF signals reflected by the soil surface. However, these approaches usually have coarse-grained geographical sensing resolutions, and could only estimate the surface moisture of the soil. A very recent RF-based technique CoMEt [18] exploits the RF signals reflected by the boundaries between the adjacent soil layers with different moisture contents, and achieves a much finer-grained geographical sensing resolution, as well as larger sensing depth than the remote sensing approaches. However, due to the moderate strength of the RF signals reflected by the soil layer boundaries, the operating distance between CoMEt's antenna array to the soil surface has to be less than 60cm, which prevents CoMEt from being carried by aerial mobile platforms (e.g., UAVs) to conduct wide-area soil moisture sensing.

Motivated by the above facts, we propose SoilId[1], an RF-based soil moisture sensing system that overcomes the above limitations of existing soil moisture sensing techniques. The operation mode of SoilId is illustrated in Figure 1. Specifically, SoilId deploys at predetermined measurement points battery-free in-ground reflectors (e.g., metal plates), which are buried beneath the soil surface and provide strong RF signal reflections. Furthermore, SoilId deploys a UAV that carries a COTS IR-UWB radar to cruise around the measurement points, and uses the IR-UWB radar to estimate the soil moisture at each measurement point through the RF signals reflected by both the soil surface and the reflector. In fact, the radar utilized by SoilId is a COTS IR-UWB radar with a central operation frequency of 7.29GHz. The reasons to select such type of radar come from its compactness in size, its lower cost compared with professional RF-based soil moisture sensing devices (e.g., ground penetrating radars [19]), as well as its sufficient soil penetrating capability validated by a series of experiments[2] that we carefully

[1]The name SoilId comes from our overall approach of Soil moisture estimation using IR-UWB radar and deep learning.
[2]Please refer to Section 2.1 for our experimental designs and results on radar choices.

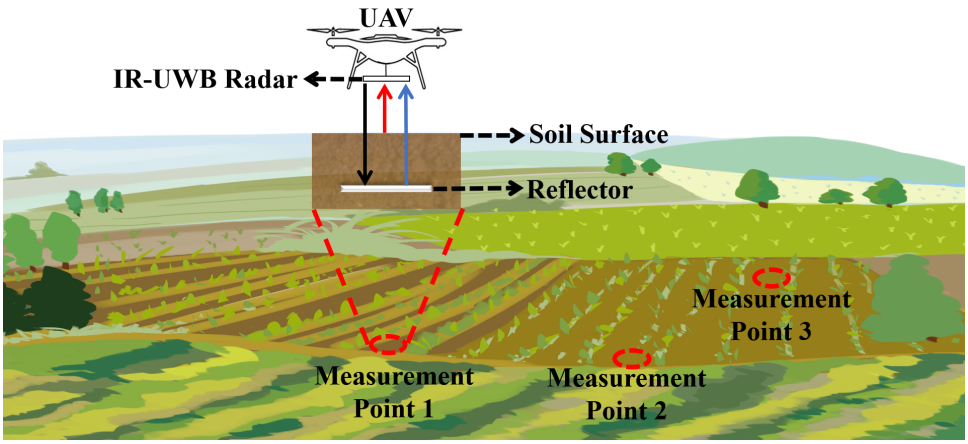

Fig. 1. Operation mode of SoilId.

conducted. In what follows, we elaborate on the challenges of designing SoilId, as well as our approaches that address them.

The first challenge comes from the discrete sampled form of the received radar signals. Specifically, SoilId estimates the soil moisture through various moisture related radar signal features, which are extracted from the basic information of the received radar signals, including the time of flights (ToFs) and amplitudes. However, the limited sampling rate of the received radar signals makes the precision of the obtained ToFs and amplitudes unsatisfactory for soil moisture sensing. To address this challenge, SoilId up-samples the received signals via interpolation, and obtains ToF estimations with a higher precision and more accurate amplitudes from the interpolated signal, which finally promotes the precision of the extracted soil moisture related features.

The second challenge is that, although the UAV enables SoilId to be highly mobile, the uncontrollable motion of it (e.g., shaking, deviating from the measurement point) will heavily contaminate part of the received signals, making them unusable for soil moisture estimation. To address this challenge, SoilId detects and filters out the distorted collected data caused by the UAV's uncontrollable motion by employing a *distorted data filtering* algorithm. The algorithm automatically filters out the distorted radar signal data according to the representative signal features when the UAV is under undesirable motion, and thus prevents them from influencing the soil moisture estimation accuracy.

In practice, however, apart from the uncontrollable motion of the UAV, the multipath interference provided by the reflections from the objects other than the reflector, such as the stones and bushes around the measurement points, could also contaminate the received radar signals. To address this challenge, SoilId leverages the mobile nature of the UAV to collect data at different altitudes, and further employs a *multipath interference elimination* algorithm that helps SoilId distinguish and discard the data distorted by multipath interference through carefully comparing the characteristics of the radar signal data received when the UAV is at different altitudes.

After SoilId filters out the data contaminated by both the UAV's uncontrollable motion and multipath interference, another challenge that arises is how to map the extracted radar signal features to accurate soil moisture estimations. Instead of simply applying the existing empirical equations (e.g., Topp equation [20]) which use polynomials to fit such mapping, SoilId leverages the powerful representation ability of deep neural networks and employs a carefully designed neural network structure, SoilIdNet, to capture the inherent relationships between the extracted radar signal features and soil moisture estimations. Furthermore, to avoid the tedious process of collecting a large volume of training data and training SoilIdNet from scratch for each type of soil,

SoilId augments the existing meta learning framework to pretrain a meta model, named as mSoilIdNet, which can be fine-tuned to fit any soil type with only a small number of labeled data.

In summary, this paper makes the following contributions.

- In this paper, we design and implement a novel RF-based soil moisture sensing system, named as SoilId, that combines a UAV and an IR-UWB radar, which is able to quickly perform wide-area soil moisture sensing without burying any in-ground battery-powered devices.
- Technically, we design a series of novel approaches that make use of the highly mobile nature of the UAV, and meanwhile eliminate the negative influences of the UAV's uncontrollable motion and the multipath interference. We envision that these approaches could potentially be useful in other UAV-based radar sensing tasks, as well.
- Furthermore, we propose a novel deep neural network model, named as SoilIdNet, to map the extracted radar signal features to soil moisture estimations, and also augment the meta learning framework to obtain a meta model, named as mSoilIdNet, which can be quickly fine-tuned to any target soil type with only a small number of labeled data.
- Finally, we conduct extensive experiments to evaluate SoilId against a variety of real-world factors, including the UAV's uncontrollable motion, the multipath interference, soil surface coverage, and many others. Our experimental results validate that SoilId can push the accuracy limits of RF-based soil moisture sensing techniques to a 50% quantile MAE of 0.23% on the tests carried out by our UAV-based system.

2 PRELIMINARIES

In this section, we first introduce the principles and the experiments to select a proper radar for soil moisture sensing. Next, we model the propagation process of the radar signal and extract the soil moisture related radar signal features for subsequent soil moisture estimation tasks.

2.1 Radar Choices

In order to select a proper radar that can be carried on a UAV for soil moisture sensing, we survey the miniature on-chip radars in the market for their compact size and light weight, and carry out a set of experiments on the soil penetrating capabilities of these radars. Specifically, we test three kinds of COTS radars with central operation frequencies of 77GHz, 24GHz, and 7.29GHz, which covers those of a wide majority of commercial COTS radars. In our experiments, the radar is placed 1m above the soil surface with the antenna plane parallel to the soil surface, and an aluminum plate is buried 30cm below the soil surface as the reflector[3]. We conduct the experiments on four types of soil, including sand, loamy soil, silt soil, and clay soil. As the experimental results for these different types of soil show similar trends, we only present those for sand as follows for conciseness.

For each of the two FMCW radars, we set it to consecutively transmit 128 chirps and apply Fast Fourier Transform (FFT) to the Intermediate Frequency (IF) signals of each chirp. Then, we stack the frequency spectrums of the 128 chirps, as illustrated in Figures 2a and 2b. The horizontal axes in these figures represent the normalized distance calculated by multiplying the ToFs of the received signals with the velocity of light in vacuum. Considering the propagation velocity of radar signals in the sand, if a radar could receive the signal reflected by the aluminum plate, there will exist a peak at the normalized distances of around 1.5m. However, we could not observe such peaks in Figures 2a and 2b, which indicates that the FMCW radars tested in our experiments cannot receive the signals reflected by the aluminum plate. This is because the signals transmitted by the aforementioned two FMCW radars attenuates rapidly in the soil due to their high frequencies, and thus the signals received by them are mostly composed of those reflected by the soil surface. For the IR-UWB radar, we obtain the amplitudes of the

[3]The reflector can be composed of other materials, such as stainless steel, as long as it can provide enough reflection to radar signals. We have conducted experiments to test the performance of reflectors of different materials in Section 6.4.5.

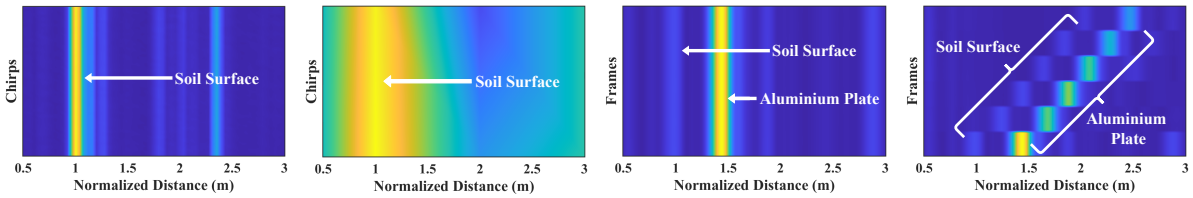

(a) FMCW radar: 77GHz. (b) FMCW radar: 24GHz. (c) IR-UWB radar: 7.29GHz. (d) IR-UWB radar at different altitudes.

Fig. 2. Experimental results on the soil-penetrating abilities of three types of commercial miniature on-chip radars with their central operation frequencies specified. The brighter zones indicate higher RSS values for the FMCW radars or larger amplitudes of the received signals for the IR-UWB radar.

received signals for 100 consecutive frames and also stack them together. From Figure 2c, we could easily observe the peaks at the normalized distances of both 1m and 1.5m, which means that the IR-UWB radar receives clear reflections from both the soil surface and aluminum plate. Additionally, we change the distance from the IR-UWB radar to the soil surface from 1m to 2m and obtain the amplitudes of the received signals for 20 consecutive frames at each distance. As is shown in Figure 2d, even if the IR-UWB radar is 2m above the soil surface, it can still clearly receive the signals reflected by the aluminum plate.

The above experiments show that the IR-UWB radar with central operation frequency 7.29GHz is able to penetrate the soil of enough depth (30cm) for moisture sensing, and from an altitude that is proper for UAV cruising (2m). Thus, we choose such IR-UWB radar as the sensing device for our soil moisture sensing task.

2.2 Modeling IR-UWB Radar Signals

In this section, we model the propagation of the IR-UWB radar signals in the process of soil moisture sensing. The IR-UWB radar carried by the UAV cruising in the air transmits pulse signals and collects the reflected signals from both the soil surface and buried reflector. The baseband signal $s(t)$ of the IR-UWB radar takes the form of Gaussian pulse, i.e.,

$$s(t) = \alpha_{tx} e^{\frac{-t^2}{2\sigma^2}}, \tag{1}$$

where α_{tx} is the amplitude determining the pulse strength and σ^2 is the variance determining the pulse width. The baseband signal is modulated to the carrier with central frequency f_c and becomes the transmitted signal

$$x(t) = s(t) e^{-j2\pi f_c t}. \tag{2}$$

Suppose the distance from the radar to the soil surface is d_1, the signal reflected by the soil surface becomes

$$r_1(t) = \alpha_1 s\left(t - \frac{2d_1}{c}\right) e^{-j2\pi f_c (t - \frac{2d_1}{c})} \frac{n-1}{n+1}, \tag{3}$$

where $\alpha_1 = e^{-2\alpha_{air} d_1}$ is the attenuation of signal propagation in the air with α_{air} denoting the attenuation factor of the air, and n is the refractive index (RI) of the soil.

Similarly, suppose the reflector is buried at a depth of d_2, then the signal reflected by the reflector can be expressed as

$$r_2(t) = \alpha_1 \alpha_2 \alpha_3 s\left(t - \frac{2(d_1 + d_2 n)}{c}\right) e^{-j2\pi f_c (t - \frac{2(d_1 + d_2 n)}{c})}, \tag{4}$$

where $\alpha_2 = e^{-2\alpha_s d_2}$ is the attenuation of signal propagation in the soil with α_s denoting the attenuation factor of the soil, and $\alpha_3 = 4n(m-n)/((n+1)^2(m+n))$ with m denoting the RI of the reflector. In fact, α_3 is the attenuation caused by penetrating the soil-air boundary and the reflection by the reflector.

2.3 Soil Moisture and IR-UWB Radar Signals

After modeling the signals reflected by the soil surface and the reflector, we then aim to find the features of signals that are related to the soil moisture. The first feature that we exploit is n, i.e., the RI of the soil. Specifically, n is defined by the ratio of the propagation velocity of the IR-UWB signals in vacuum to that in the soil. In fact, the value of n is influenced by the relative permittivity and electrical conductivity of the soil, both of which are closely related to the soil moisture [21].

Apart from n, another feature influenced by the soil moisture is the in-soil attenuation factor α_s [10]. Specifically, α_s influences $r_2(t)$'s peak amplitude, i.e., $\alpha_1\alpha_3 e^{-2\alpha_s d_2}$. However, this value is also influenced by other parameters that are hard to obtain, such as the in-air attenuation α_1, and thus, we cannot directly calculate α_s from $r_2(t)$'s peak amplitude. In fact, from Equations (3) and (4), we notice that the signals $r_1(t)$ and $r_2(t)$ are both attenuated by α_1 because of the same signal propagation distance in the air. Thus, we can utilize this property and obtain the *relative amplitude ratio (RAR)* defined in the following Definition 1, which does not depend on the in-air signal propagation process but is related to α_s.

Definition 1 (Relative Amplitude Ratio). *The relative amplitude ratio p is defined as the ratio of $r_2(t)$'s peak amplitude (i.e., $\alpha_1\alpha_2\alpha_3$) to $r_1(t)$'s peak amplitude (i.e., $\alpha_1(n-1)/(n+1)$). That is,*

$$p = \frac{\alpha_2\alpha_3(n+1)}{n-1} = e^{-2\alpha_s d_2}\frac{4n(m-n)}{(m+n)(n+1)(n-1)}. \tag{5}$$

By Definition 1, if we fix the material of the reflector and its buried depth, which leads to fixed m and d_2, the value p will only be determined by α_s and n.

Thus, based on the above discussions in Section 2.3, we choose to use the soil RI n and RAR p extracted from the IR-UWB radar signals as the features to estimate the soil moisture, as elaborated in Section 4.1.

3 METHODOLOGY OVERVIEW

In this paper, we propose to use an IR-UWB radar carried by a UAV to sense the soil moisture. Figure 3 shows an overview of our proposed methodology, referred to as SoilId, which contains three major components: (1) data collection, (2) feature extraction and data selection, and (3) moisture estimation via neural network.

- **Data Collection.** The function of this component is to collect the IR-UWB radar signals that can be used to estimate the soil moisture. We first select several representative measurement points in the sensing area[4]. At each measurement point, we bury in advance a reflector that is highly reflective to the IR-UWB radar signals (e.g., an aluminum plate) under the soil surface at a specific depth. During the data collection process, the UAV hovers above each measurement point, and raises its altitude vertically within a pre-defined altitude range. Meanwhile, the IR-UWB radar attached on the UAV collects the reflected signals continuously. Such design of vertical raise of the UAV's altitude is to resolve the multipath interference problem which will be elaborated in Section 4.3.
- **Feature Extraction and Data Selection.** This component extracts soil moisture related features (i.e., soil RI and RAR) from the received radar signals, and selects the valid data that can be fed to our soil moisture estimation model. Specifically, we first perform interpolation to acquire more accurate amplitudes and ToFs of the received signals (Section 4.1). After that, we filter out the unusable data distorted by the uncontrollable motion of the UAV (Section 4.2). Next, we detect and discard the data influenced by multipath interference (Section 4.3). The extracted features of the remaining data are used for soil moisture estimation.

[4]In practice, it suffices to measure the soil moisture only at a few representative points, as the moisture distribution of the entire sensing area could usually be estimated using the samples taken at several measurement points using existing methods, such as [22–24]. However, the method of choosing the measurement points are out of the scope of this paper.

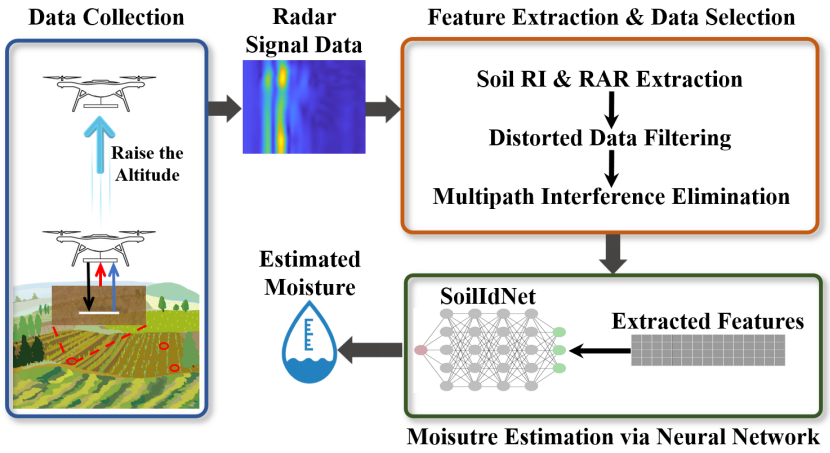

Fig. 3. System overview of SoilId, where the red circles indicate the measurement points in the sensing area.

- **Moisture Estimation via Neural Network.** This component is designed to estimate the soil moisture through the extracted radar signal features. To achieve this goal, we propose a neural network model that can directly map the input features to the estimated soil moisture (Section 5.1). Besides, it is typically tedious to collect a large volume of labeled training data to fit the neural network model for a new type of soil. Thus, we propose to augment the meta learning framework to enable fast adaptation from the model trained on existing soil types to the target new soil type with only few labeled training data (Section 5.2).

In the following parts of this paper, we will mainly elaborate upon the feature extraction and data selection, as well as moisture estimation via neural network components in Sections 4 and 5.

4 FEATURE EXTRACTION AND DATA SELECTION

In this section, we first introduce how to accurately extract the RAR and soil RI from the received radar signals. Then, we discuss the problem that the UAV's motion and the multipath interference contaminate the received radar signal, as well as our proposed distorted data filtering and multipath elimination algorithm to solve it.

4.1 RAR and Soil RI Extraction

In order to extract the RAR and soil RI from the received radar signals, we need to obtain the ToFs[5] and peak amplitudes of $r_1(t)$ and $r_2(t)$. However, the signals we can collect from the IR-UWB radar are actually the discrete sampled version of the continuous received signals. The time interval between two consecutive samples is 0.343ns, which is also the ToF precision. However, if the distance from the radar to the soil surface is 1m, which is proper for a UAV to hover over the measurement point, we can easily calculate that the ToF of $r_1(t)$ is about 6.67ns. As a result, such a precision is unsatisfactory for accurate ToF calculation, because it is over 5% of the ToF itself. Besides, the sampling points do not necessarily coincide with the peaks of $r_1(t)$ and $r_2(t)$, so that the obtained peak amplitudes are imprecise, as well.

In order to obtain more accurate ToFs and peak amplitudes of $r_1(t)$ and $r_2(t)$, we propose to up-sample the received signals via interpolation. Specifically, as illustrated in Figure 4, we apply spline interpolation[6] on the

[5]In this paper, we define the ToF of a pulse signal as the ToF of the signal point with the peak amplitude.
[6]We have also implemented other interpolation techniques, such as low-pass filtering, and they have similar performances with spline interpolation.

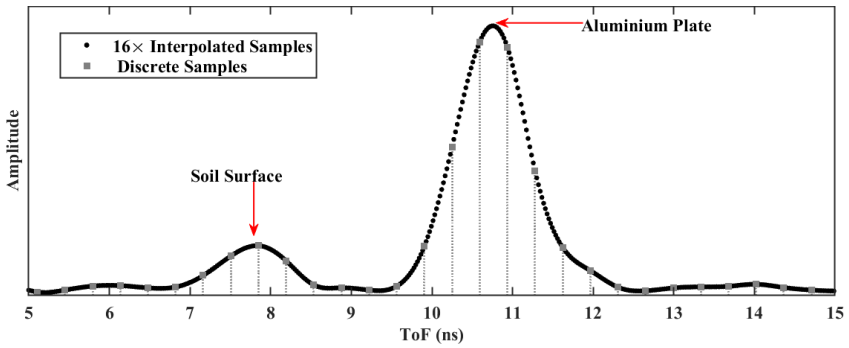

Fig. 4. Interpolation of the sampled received signals of the IR-UWB radar.

amplitudes of the collected sampled signals. In fact, we perform 16× interpolation in our experiments, promoting the ToF precision to 21.3 ps. Such a precision is sufficient, as it is within 0.5% of the ToF values of $r_1(t)$ and $r_2(t)$.

Suppose the IR-UWB radar receives totally k frames of signals at a measurement point. We then apply interpolation on the signals of each frame. After that, we calculate the values of the soil RI and RAR of each frame by the following process. For the ith frame, we first find the samples of $r_1(t)$ and $r_2(t)$ with the highest amplitudes, and obtain the amplitudes $a_{1,i}$ and $a_{2,i}$ and ToFs $t_{1,i}$ and $t_{2,i}$ of these two samples. The values of the soil RI and RAR that correspond to the ith frame are then calculated as $n_i = 0.5c(t_{2,i} - t_{1,i})/d_2$ and $p_i = a_{2,i}/a_{1,i}$, respectively. We apply such process to all of the k received frames and obtain the sets of peak amplitudes of $r_1(t)$ and $r_2(t)$, soil RI, and RAR of each frame, denoted as $\mathcal{A}_1 = \{a_{1,1}, a_{1,2}, \cdots, a_{1,k}\}$, $\mathcal{A}_2 = \{a_{2,1}, a_{2,2}, \cdots, a_{2,k}\}$, $\mathcal{N} = \{n_1, n_2, \cdots, n_k\}$, and $\mathcal{P} = \{p_1, p_2, \cdots, p_k\}$. These sets of values are further used for distorted data filtering as described in the following Section 4.2.

4.2 Distorted Data Filtering

4.2.1 Illustration of Data Distortions. The uncontrollable motion of the UAV makes part of the received signals contaminated and thus unable to be directly used for soil moisture estimation. To illustrate this problem, we choose three pieces of representative data collected by the IR-UWB radar attached on the UAV at the same measurement point. Each piece of data contains 240 consecutive frames. We apply the interpolation technique as described in Section 4.1 to each frame and plot their amplitudes as illustrated in Figure 5.

The data for Figure 5a is collected by the IR-UWB radar attached on a UAV stably hovering above the measurement point (State S1). From Figure 5a, we observe that the peak amplitudes and the ToFs of $r_1(t)$ and $r_2(t)$ are quite steady. Figures 5b and 5c show two representative distorted data caused by the undesirable motion of the UAV. As illustrated in Figure 5b, when the UAV is shaking (State S2), the orientation of the UAV will change rapidly, which makes the antenna plane of the IR-UWB radar not always parallel to the soil surface, and thus causes frequent change to the peak amplitudes of $r_1(t)$ and $r_2(t)$. Figure 5c shows the scenario where the UAV deviates from the measurement point (State S3). In such case, the transmitted signal will not be reflected by the reflector. Thus, the peak amplitudes of $r_2(t)$ is becoming much smaller and gradually disappears as the UAV deviates from the measurement point.

4.2.2 Distorted Data Filtering Algorithm. Based on the above observations, we design the distorted data filtering algorithm as elaborated in Algorithm 1 to detect and discard the data distorted by the UAV's undesirable motion for each measurement point. The algorithm takes the four sets $\mathcal{A}_1$, $\mathcal{A}_2$, $\mathcal{N}$ and $\mathcal{P}$ extracted using the technique in Section 4.1, as well as the sliding window size h, outlier detection threshold δ as inputs, and outputs the sets of filtered soil RIs $\mathcal{N}'$ and RARs $\mathcal{P}'$.

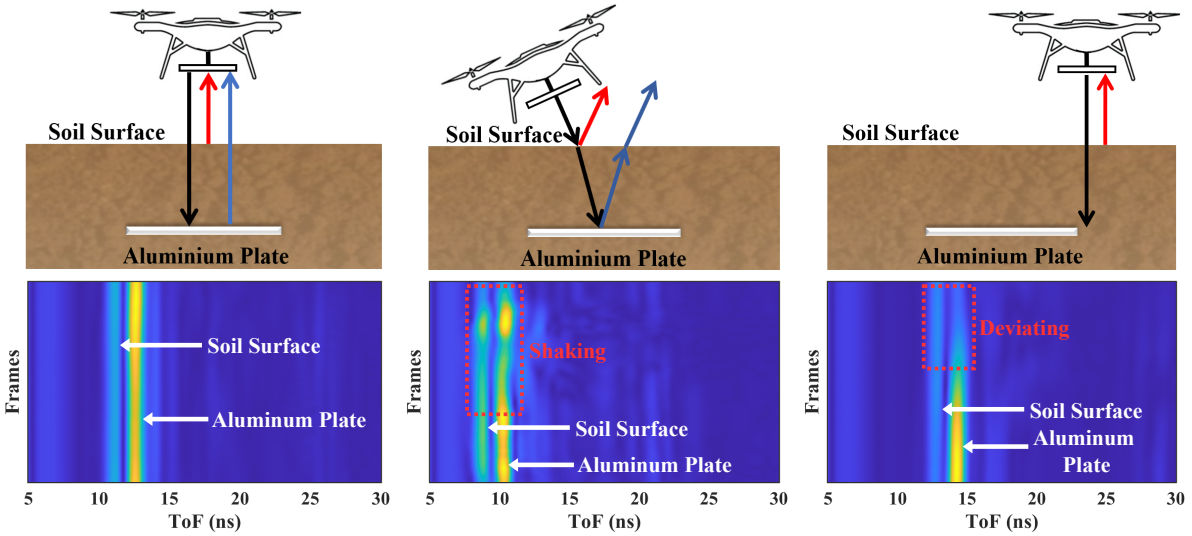

(a) The scenario where the UAV is stably hovering the measurement point and the corresponding received radar signals.

(b) The scenario where the UAV is shaking above the measurement point and the corresponding received radar signals.

(c) The scenario where the UAV is deviating from the measurement point and the corresponding received radar signals.

Fig. 5. Examples of the flight state of the UAV and the corresponding received signals of IR-UWB radar, where the black, red, and blue arrow represents the signal transmitted by the IR-UWB radar, reflected by the soil surface, and reflected by the aluminum plate, respectively.

Algorithm 1: Distorted Data Filtering Algorithm

Input: $\mathcal{A}_1$, $\mathcal{A}_2$, $\mathcal{N}$, $\mathcal{P}$, h, δ;
Output: Sets of filtered soil RIs $\mathcal{N}'$ and RARs $\mathcal{P}'$;
// Initialization.
1 $\mathcal{N}' \leftarrow \emptyset, \mathcal{P}' \leftarrow \emptyset$;
// Peak amplitude averages calculation.
2 $\overline{a}_1 \leftarrow \frac{1}{|\mathcal{A}_1|} \sum_{i:a_{1,i} \in \mathcal{A}_1} a_{1,i}, \overline{a}_2 \leftarrow \frac{1}{|\mathcal{A}_2|} \sum_{i:a_{2,i} \in \mathcal{A}_2} a_{2,i}$;
// Data selection.
3 **for** $i = 1 + h$ *to* $k - h$ **do**
  // RAR Moving averages calculation.
4 $m_{i,1} \leftarrow \frac{1}{h} \sum_{j=i-h}^{i-1} p_j, m_{i,2} \leftarrow \frac{1}{h} \sum_{j=i+1}^{i+h} p_j$;
5 **if** $|p_i - m_{i,1}| < \delta$ *and* $|p_i - m_{i,2}| < \delta$ *and* $a_{i,1} > \overline{a}_1$ *and* $a_{i,2} > \overline{a}_2$ **then**
6 $\mathcal{N}' \leftarrow \mathcal{N}' \bigcup \{n_i\}, \mathcal{P}' \leftarrow \mathcal{P}' \bigcup \{p_i\}$;

After initializing the sets $\mathcal{N}'$ and $\mathcal{P}'$ as empty (line 1), the algorithm calculates the average peak amplitudes of $r_1(t)$ and $r_2(t)$ of each frame (line 2). Next, for each of the ith frame with $i \in [1 + h, k - h]$, the algorithm checks whether it is usable (lines 3-6). The algorithm first calculates the moving average $m_{i,1}$ and $m_{i,2}$ of the RARs in h previous frames and h subsequent frames (line 4). If the ith frame is collected when the UAV is stable, the extracted RAR will have similar values as those calculated RAR moving averages $m_{i,1}$ and $m_{i,2}$, which means conditions $|p_i - m_{i,1}| < \delta$ and $|p_i - m_{i,2}| < \delta$ should hold. Besides, if the UAV does not deviates from the measurement point,

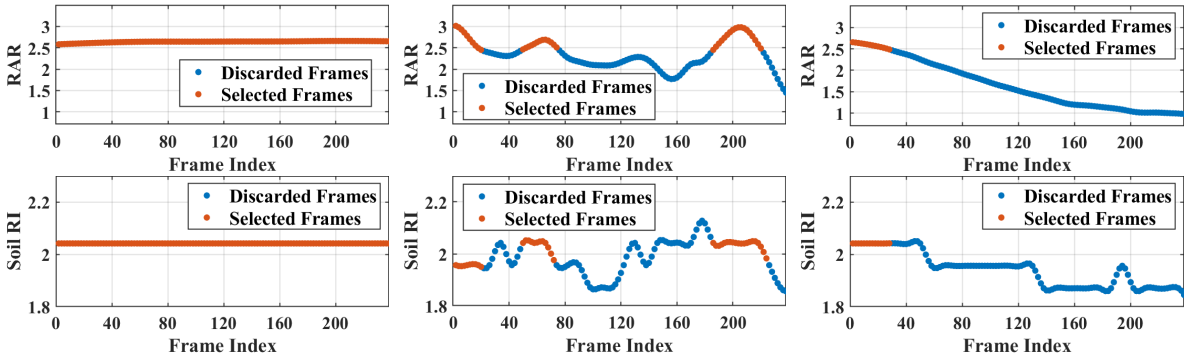

(a) S1. (b) S2. (c) S3.

Fig. 6. Frames of RARs and soil RIs selected and discarded by Algorithm 1 under UAV flight states S1, S2 and S3.

the peak amplitudes of $r_1(t)$ and $r_2(t)$ should be no less than the calculated average peak amplitudes over all the frames, which means conditions $a_{i,1} > \overline{a}_1$ and $a_{i,2} > \overline{a}_2$ should hold. Therefore, the algorithm retains the soil RI and RAR of the ith frame, if all the aforementioned four conditions are satisfied (line 5-6).

Figure 6 demonstrates the frames of RARs and soil RIs discarded and selected by Algorithm 1, when it takes the RARs and soil RIs extracted from the frames collected at the same measurement point under different UAV flight states S1, S2, and S3, as shown in Figure 5. The values of RARs and soil RIs extracted from all the frames under S1 are in consensus and they are all selected by Algorithm 1. When Algorithm 1 takes the RARs and soil RIs extracted from the frames collected under S2 or S3, it only selects the frames whose values of RARs and soil RIs are similar to those extracted from frames collected under S1. Specifically, suppose that the average extracted RAR and soil RI under S1 are $\overline{p}_{S1}$ and $\overline{n}_{S1}$, the sets of RARs extracted under S2 and S3 are $\mathcal{P}_{S2}$ and $\mathcal{P}_{S3}$, and the sets of soil RIs extracted under S2 and S3 are $\mathcal{N}_{S2}$ and $\mathcal{N}_{S3}$, respectively. After the selection of Algorithm 1, suppose that the sets of selected RARs under S2 and S3 are $\mathcal{P}'_{S2}$ and $\mathcal{P}'_{S3}$, and the sets of selected soil RIs under S2 and S3 are $\mathcal{N}'_{S2}$ and $\mathcal{N}'_{S3}$. We further define $E(\mathcal{K}, f) = \frac{1}{|\mathcal{K}|}\sum_{k\in\mathcal{K}}|k - f|$ as the mean absolute errors (MAEs) between elements in set $\mathcal{K}$ and f. The values of $E(\mathcal{P}'_{S2}, \overline{p}_{S1})$ and $E(\mathcal{P}'_{S3}, \overline{p}_{S1})$ are only 0.149 and 0.063, whereas those of $E(\mathcal{P}_{S2}, \overline{p}_{S1})$ and $E(\mathcal{P}_{S3}, \overline{p}_{S1})$ raise to 0.395 and 1.001. Similarly, the values of $E(\mathcal{N}'_{S2}, \overline{n}_{S1})$ and $E(\mathcal{N}'_{S3}, \overline{n}_{S1})$ are only 0.028 and 0.017, whereas those of $E(\mathcal{N}_{S2}, \overline{n}_{S1})$ and $E(\mathcal{N}_{S3}, \overline{n}_{S1})$ raise to 0.062 and 0.104. The quantitative results validate the effectiveness of Algorithm 1 for automatically discarding the data contaminated by the UAV's undesirable motions.

The retained data will be further used for resolving multipath interference as elaborated in the following Section 4.3.

4.3 Multipath Interference Elimination

Apart from the UAV's undesirable motion, the multipath interference caused by the reflections from the objects other than the reflector, such as bushes and stones that may appear near the measurement point, could also contaminate the collected data. This is because the multipath signals may mix with $r_1(t)$ and $r_2(t)$, which influences the accuracy of the obtained peak amplitudes and ToF of $r_1(t)$ and $r_2(t)$, and further makes the extracted soil RI and RAR unusable for accurate soil moisture sensing.

Our insights to resolve such multipath interference is by leveraging the mobile nature of the UAV. Specifically, as mentioned in Section 3, we let the UAV hover over each measurement point and raise its altitude vertically within a predefined range. In practice, multipath interference only happens when the UAV is at some specific

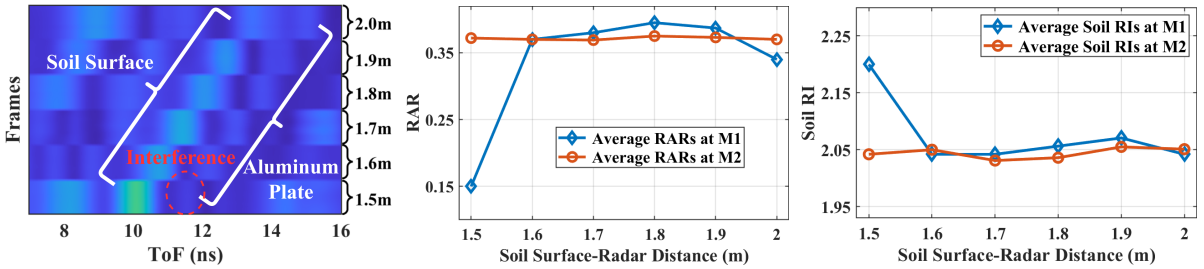

(a) Received radar signals at M1. (b) Average RARs. (c) Average soil RIs.

Fig. 7. Received radar signals, average RARs and soil RIs at different soil surface-radar distance.

altitudes where the Gaussian pulses of the interference signals overlap with $r_1(t)$ and $r_2(t)$. Thus, only at certain altitudes during the raising process, the received frames will be influenced by multipath interference.

We validate the above insights by carrying out experiments at a measurement point M1 in a garden with plenty of bushes and trees to provide rich multipath reflections. We change the distance from the IR-UWB radar to the soil surface vertically from 1.5m to 2m in a 10cm increment, and plot the received signals and average RARs and soil RIs of the frames collected at each altitude in Figure 7. From Figure 7a, we notice that when the distance from the IR-UWB radar to the soil surface is 1.5m, the peak amplitude of $r_2(t)$ is abnormally low, and the ToF difference between $r_1(t)$ and $r_2(t)$ is abnormally large, which lead to the calculated average RAR and soil RI with abnormal values, as shown in Figure 7b and 7c, compared with those RARs and soil RIs at higher altitudes.

Based on the above insights and experimental results, we design the multipath interference elimination algorithm as elaborated in Algorithm 2. The algorithm takes the sets of filtered soil RIs $\mathcal{N}'$ and RARs $\mathcal{P}'$ output by Algorithm 1, as well as the outlier detection thresholds ϵ_n and ϵ_p as inputs, and outputs the sets of valid soil RIs $\mathcal{N}''$ and RARs $\mathcal{P}''$. At first, the algorithm initializes the sets $\mathcal{N}''$ and $\mathcal{P}''$ as empty (line 1). After that, the algorithm first calculates the averages of the soil RIs $\overline{n}$ and RARs $\overline{p}$ in the input sets $\mathcal{N}'$ and $\mathcal{P}'$ (line 2). Next, the algorithm checks every pair of (n_i, p_i) to evaluate whether their values are influenced by multipath interference (lines 3-5). Since in practice multipath interference only occurs to few frames, the average of soil RIs and RARs across all the frames should be close to those without multipath interference. Thus, the algorithm regards the pair (n_i, p_i) as valid and keeps it, only if n_i, and p_i do not deviate from the averages $\overline{n}$ and $\overline{p}$ too much, i.e., the conditions $|n_i - \overline{n}| < \epsilon_n$ and $|p_i - \overline{p}| < \epsilon_p$ hold (lines 4-5).

To evaluate the effectiveness of Algorithm 2, we manually collect the soil at the measurement point M1, and construct another measurement point M2 with the collected soil in a multipath free environment. We then collect

Algorithm 2: Multipath Interference Resolving Algorithm

Input: $\mathcal{N}', \mathcal{P}', \epsilon_n, \epsilon_p$;
Output: Sets of valid soil RIs $\mathcal{N}''$ and RARs $\mathcal{P}''$;
// Initialization.
1 $\mathcal{N}'' \leftarrow \emptyset, \mathcal{P}'' \leftarrow \emptyset$;
// Average RI and RAR calculation.
2 $\overline{n} \leftarrow \frac{1}{|\mathcal{N}'|} \sum_{i:n_i \in \mathcal{N}'} n_i, \overline{p} \leftarrow \frac{1}{|\mathcal{P}'|} \sum_{i:p_i \in \mathcal{P}'} p_i$;
// Data selection.
3 **for** $i = 1$ *to* $|\mathcal{N}'|$ **do**
4 **if** $|n_i - \overline{n}| < \epsilon_n$ *and* $|p_i - \overline{p}| < \epsilon_p$ **then**
5 $\mathcal{N}'' \leftarrow \mathcal{N}'' \bigcup \{n_i\}, \mathcal{P}'' \leftarrow \mathcal{P}'' \bigcup \{p_i\}$;

the IR-UWB radar signal at M2 following the same procedure at M1 and extract the RARs and soil RIs. Figure 7b and 7c indicate that the averages of RARs and soil RIs extracted from the signals collected at M1 and M2 are similar at most soil surface-radar distance, except for at the height of 1.5m, where the signal collected at M1 are interfered by the multipath signal. For RARs and soil RIs at M1, Algorithm 2 discards those at the soil surface-radar distance of 1.5m and retains the others. Specifically, suppose that the average extracted RAR and soil RI at M2 are $\overline{p}_{M2}$ and $\overline{n}_{M2}$, and the sets of extracted RARs and soil RIs at M1 are $\mathcal{P}'_{M1}$ and $\mathcal{N}'_{M1}$, respectively. After the selection of Algorithm 2, suppose the sets of selected RARs and soil RIs at M1 are $\mathcal{P}''_{M1}$ and $\mathcal{N}''_{M1}$. The values of $E(\mathcal{P}''_{M1}, \overline{p}_{M2})$ and $E(\mathcal{N}''_{M1}, \overline{n}_{M2})$ are only 0.0125 and 0.0127, whereas those of $E(\mathcal{P}'_{M1}, \overline{p}_{M2})$ and $E(\mathcal{N}'_{M1}, \overline{n}_{M2})$ raise to 0.0495 and 0.0372. The quantitative results validate the effectiveness of Algorithm 2 for automatically discarding the data contaminated by multipath interference.

After the multipath interference elimination process, the retained data will be further used for soil moisture estimation introduced in the following Section 5.

5 MOISTURE ESTIMATION VIA NEURAL NETWORKS

In this section, we introduce the proposed novel deep neural network, SoilIdNet, that directly maps the input radar signal features to soil moisture. After that, we elaborate on augmenting the mata learning framework to enable fast adaptation from the pretrained meta model, mSoilIdNet, to the new target soil type with only a few labeled training data.

5.1 Deep Neural Network Model

Although there exist some empirical equations (e.g., Topp equation [20]) that offer mappings from certain physical properties (e.g., apparent permittivity) of the soil to its moisture, these equations usually use simple polynomials to fit such mappings, which have limited representation ability, and thus suffer from unsatisfactory moisture estimation accuracy. Alternatively, we leverage the powerful representation ability of neural networks, and design a neural network structure (named as SoilIdNet), which uses Multi-Layer Perception (MLP) as its basic building block, to directly map the extracted radar signal features to soil moisture. Basically, SoilIdNet consists of three modules, i.e., two encoder modules and one inference module. The two encoder modules take respectively the RARs and soil RIs as inputs and encode the input data. The inference model then jointly takes the output of the two encoder modules as input and yields the soil moisture estimations. Compared with Topp equation that only relies on the soil RIs for moisture estimation, the inference module fully utilizes the rich soil moisture related information extracted from both RARs and soil RIs, which further promotes the sensing accuracy.

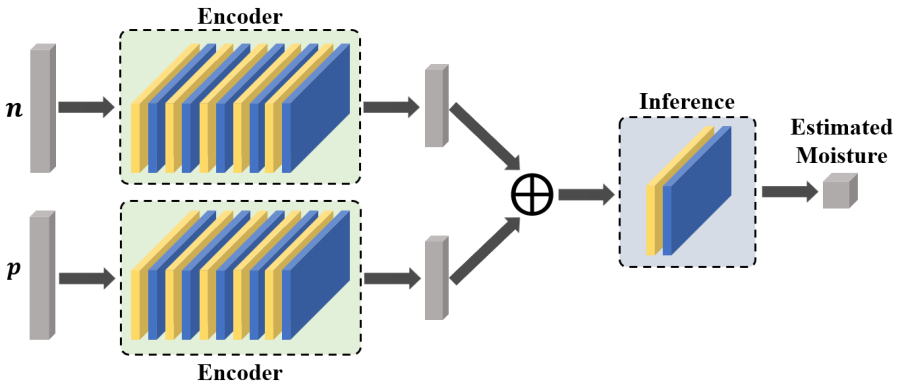

Fig. 8. Structure of our SoilIdNet. The blue blocks indicate the FC layers, the yellow blocks indicate the ReLU layers, and ⊕ indicates the concatenation operation.

After the process of feature extraction and data selection described in Section 4, we randomly select K soil RIs from $\mathcal{N}''$ and K RARs from $\mathcal{P}''$, and then gather them respectively into two K dimensional vectors, denoted as $\mathbf{n}$ and $\mathbf{p}$. As illustrated in Figure 8, $\mathbf{n}$ and $\mathbf{p}$ are fed into two encoder modules respectively. Each encoder module is an MLP that consists of alternating fully connected (FC) and ReLU activation layers. Then, the features output by the encoder modules are concatenated and fed into the inference module which is also an MLP composed of alternating FC and ReLU activation layers. The inference module finally outputs the soil moisture estimation.

Given enough training data[7] collected over one type of soil, we could train SoilIdNet for such soil type by minimizing the MAE loss between the estimated soil moisture and ground truth. However, due to the variant physical properties of different types of soil, our SoilIdNet trained on one soil type does not necessarily perform satisfactorily on others. Moreover, it is clearly tedious to collect a large volume of labeled training data to train an SoilIdNet model individually for each soil type. To mitigate this issue, we propose to augment the meta learning framework with details elaborated in the following Section 5.2.

5.2 Meta Learning for Fast Adaptation

In real practice, soil moisture sensing tasks are conducted on a variety of types of soil, which have variant components, particle sizes, as well as water holding abilities. To avoid complete retraining of SoilIdNet for every type of soil that we may encounter in real-world tests, we propose to pretrain a meta model (named as mSoilIdNet), which is an instance of SoilIdNet with parameters that can be fine-tuned to fit any new encountered soil type with only a small number of labeled training data and a few gradient descent steps.

5.2.1 Meta Model Training. To obtain mSoilIdNet, a straightforward way is to adopt the existing meta learning framework MAML [25] to train a model that is suitable to construct the latent representations of the input radar signal features for different types of soil. However, directly applying MAML is problematic in our scenario, and we elaborate the reasons as follows. In each training epoch, MAML uses a set of training data sampled randomly from the entire training dataset of all soil types. However, such a mixed-soil-type training data generation policy is problematic for mSoilIdNet to learn the essential variation trend of RAR and soil RI when the moisture of a single type of soil varies, as the soil type is agnostic to mSoilIdNet in meta training process. Therefore, to alleviate such problem, we augment MAML by strictly sampling the training data used in the same epoch from those collected over the same type of soil, and utilize such augmented MAML to train mSoilIdNet.

5.2.2 Meta Model Adaptation. After the meta model mSoilIdNet is trained, we adapt it to the target soil type by the following process. We first (1) collect a small dataset on the target soil type under very few (as few as one or two) moisture levels. After that, we (2) fine-tune mSoilIdNet using stochastic gradient decent to minimize the MAE loss between the estimated soil moisture and ground truth, over the dataset collected in step (1).

In order to enhance the efficiency of the above adaptation process, we freeze the parameters of the encoder modules and only update those of the inference module. Our insight for such partial update method is that, through the meta model training process, the encoder modules of mSoilIdNet learn the encoding principle suitable for different types of soil. Thus, only fine-tuning the final inference module is sufficient for adaptation.

6 EXPERIMENTS

In this section, we first introduce in detail the implementation of SoilId. Next, we show the experimental setups and results for evaluating SoilId against variety real-world factors, as well as validating the adaptation ability of the meta model mSoilIdNet.

[7] Our training data collection method will be introduced in Section 6.3.

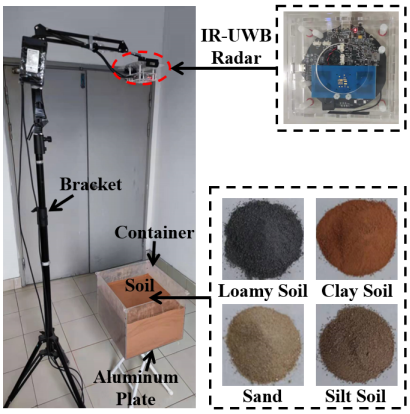

Fig. 9. Overview of the bracket-based system that collects the training data in lab environments.

Fig. 10. Overview of the UAV-based system, where the numbered components represent 1: mini PC, 2: IR-UWB radar, 3: power cable from the mini PC to the IR-UWB radar, and 4: power cable from the UAV to the mini PC.

6.1 Experimental Setup

We evaluate SoilId on four different kinds of representative soil, including sand, loamy soil, silt soil, and clay soil, which have variant components, particle sizes as well as water holding abilities. We conduct experiments in both lab environments and in the wild for field tests. For lab environments, we place the soil in a container with a size 35cm × 35cm × 30cm, which can hold the soil with a enough depth, and meanwhile the container's moderate volume makes it convenient for us to change the soil moisture and alternate different types of soil. For field tests, we measure the soil moisture at three measurement points on a lawn. In our experiments, an aluminum plate with a size 30cm × 30cm is buried below the soil surface. We choose such a reflector size to ensure that the IR-UWB radar could be easily aligned with the measurement point, which greatly facilitates the data collection process in our experiments. In practice, the reflector can be smaller to reduce cost. The reasons for selecting aluminum as the material for the reflector will be elaborated in Section 6.4.5.

We use the volumetric water content (VWC) to depict the soil moisture, which is a standard metric defined by the ratio of the volume of the water contained in the soil to the total volume of the the soil containing it. We obtain the moisture ground truths of the training datasets through the oven-based method [26], which is regarded as the most accurate method to obtain the moisture of the soil samples. Specifically, we first fill up a container with a known volume by the soil sample. Next, we weigh the soil sample and heat it in the oven for sufficiently long time to make it totally dry. Then, we reweigh the dried-up soil sample and get the weight of the water by subtracting the weight of the soil sample before and after the heating process. Finally, we calculate the volume of the water in the soil sample, and further use it to obtain the VWC value of the soil sample.

6.2 System Implementations

6.2.1 Bracket-Based System. As illustrated in Figure 9, the bracket-based system hangs an IR-UWB radar on a stable bracket to collect radar signal data. Such system prevents the collected radar signal data from being contaminated by the uncontrollable motion of the UAV, and is thus primarily used to collect the training datasets. Furthermore, we also use such bracket-based system to collect the testing datasets in a few experiments which are further discussed in Sections 6.4.1 and 6.4.3. The core component of our IR-UWB radar is the low-cost Novelda X4M05 IR-UWB transceiver [27], which transmits the baseband signal with a bandwidth of 1.5 GHz modulated

onto a 7.29GHz carrier. In such bracket-based system, the IR-UWB radar is controlled and powered by a laptop through two separate serial ports.

6.2.2 UAV-Based System. Apart from the aforementioned bracket-based system, we also implement a UAV-based system for the testing process, as is shown in Figure 10. Specifically, we use the DJI Matrix 210 UAV as the mobile platform that carries a Dell OptiPlex 7040 mini PC and the IR-UWB radar introduced in Section 6.2.1. The UAV provides power to the mini PC through its XT30 external power interface and a 24V to 19.5V voltage converter. The IR-UWB radar is further powered by the mini PC through a power serial port. Thus, we do not need to attach additional batteries on the UAV other than those that power the UAV itself. By the above system design, the total weight of the attached devices on the UAV is 1.183kg, which is less than the allowable load 1.57kg of our DJI Matrix 210 UAV. For UAVs with lower loading capacity, we can replace the mini PC by a single-board computer, such as Raspberry Pi, to decrease the weight of the system.

Apart from powering the IR-UWB radar, the mini PC also runs a piece of python script to control when the IR-UWB radar begins and stops to collect data. Such control commands are sent from the mini PC to the IR-UWB radar via a data serial port. The data collected by the IR-UWB radar is sent to the mini PC through the data serial port. Moreover, on the mini PC, we implement the RAR and soil RI extraction, distorted data filtering, and multipath interference elimination components in MATLAB and implement the neural networks of the SoilIdNet and fine-tuned mSoilIdNet in Python. The collected data can be directly processed by the mini PC, and thus, we can get the soil moisture estimation results in real time.

6.3 More Details on Training and Testing

In our experiments, to further ensure the quality of the collected training data, the bracket-based system is operated in a multipath-free environment, which helps get rid of the multipath interference. For each combination of soil type and soil moisture that we consider in our experiments, we extract the soil RIs and RARs from the received frames and collect 1000 training data instances. For moisture estimation of a single type of soil, the SoilIdNet model is trained for 2000 epochs. For meta model training, we select all the available training datasets apart from the dataset of the target soil type to train the mSoilIdNet. The meta model mSoilIdNet is trained for 4000 epochs, and in the adaptation process, it is updated for 20 epochs using the labeled data with only one or two kinds of moisture labels. All the training and adaptation procedures are conducted on a laptop with Intel i7-1160G7 CPU, and 12 GB memory. The entire training times of SoilIdNet and mSoilIdNet are around 1 hour and 3 hours. The adaptation time of mSoilIdNet is around 3 minutes.

As mentioned in Section 6.2, the testing datasets are collected by both the UAV-based system and bracket-based system. In the process of testing with the UAV-based system, the UAV raises its altitude so that the distance from the IR-UWB radar to the soil surface increases from 1m to 3m. We select such a distance range for the following three reasons. First, it ensures the received signals reflected by the soil surface and the reflector are strong enough to be distinguished from the noise. Second, it is included in the distance range (0-5m) that the UAV can rely on the altitude sensing system [28] (consisting of stereo vision sensors and ultrasonic sensors) to accurately sense its distance to the ground and further to control its altitude. Moreover, such a distance range prevents the UAV to be too close to the ground for its flight safety. For the bracket-based system, we also manually raise the distance from the radar to the soil surface to mimic the raising motion of the UAV. For each combination of soil type and soil moisture, we collect 200 testing data instances with both systems. The SoilIdNet outputs the moisture estimation of all the 200 testing data instances, and we use the average of these values as the final testing moisture estimation.

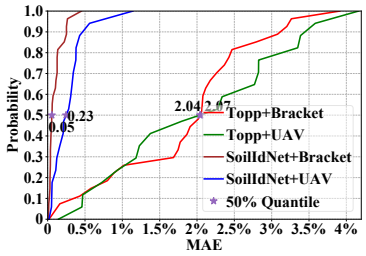

Fig. 11. CDF of the overall accuracy of SoilIdNet and the baseline method.

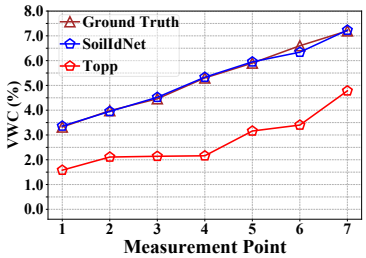

Fig. 12. Bracket tests for loamy soil.

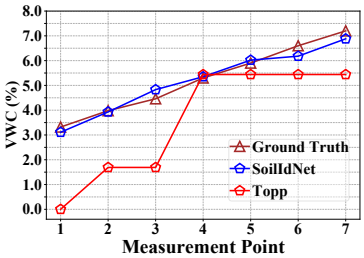

Fig. 13. UAV tests for loamy soil.

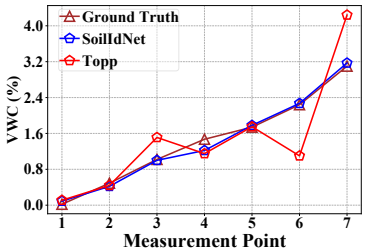

Fig. 14. Bracket tests for sand.

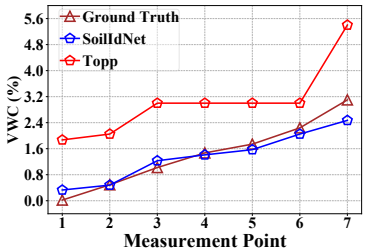

Fig. 15. UAV tests for sand.

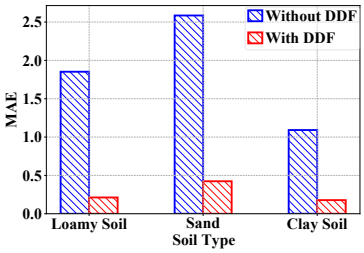

Fig. 16. MAEs of SoilIdNet with or without distorted data filtering.

6.4 Performance of SoilIdNet

6.4.1 Overall Accuracy. To evaluate the accuracy of SoilIdNet, we test it in lab environments where we can accurately control the soil moisture and designate the soil type. We evaluate the accuracy of SoilIdNet on the test datasets collected by both the bracket-based system (bracket test) and the UAV-based system (UAV test). We compare the performance of SoilIdNet against the baseline that uses Topp equation [20] to estimate the soil moisture. The Topp equation uses polynomials to fit the mappings between the extracted soil RI and soil moisture. For each combination of soil type and data collection system, we construct 7 different measurement points such that the soil moisture monotonically increases from measurement point 1 to measurement point 7.

Specifically, the errors of SoilIdNet and the baseline method are defined as the MAE between the ground truths and the estimated VWC values. Figure 11 shows the CDFs of the errors of all the experiments conducted over all four types of soil in both the bracket and UAV tests. From this figure, we could observe that for SoilIdNet the 50% quantile of VWC errors is just 0.05% in the bracket tests, and 0.23% in the UAV tests. The baseline method has much higher 50% quantile of VWC errors in both bracket tests and UAV tests, which are 2.04% and 2.07%, respectively. Clearly, the soil moisture estimation accuracy of SoilIdNet in the UAV tests is slightly lower than that in the bracket testes due to the distortion of the collected testing data caused by the UAV's uncontrollable motion and multipath interference. However, despite of such distortion and interference, our distorted data filtering and multipath interference elimination algorithms help us control the error of SoilIdNet within an acceptable range.

Besides, we show the experimental results for loamy soil and sand in both the bracket and UAV tests, and omit those for clay soil and silt soil for conciseness because they show similar trends. As illustrated in Figures 12 to 15, the errors in the bracket and UAV tests for both the loamy soil and sand show a similar trend as the overall accuracy shown in Figure 11. Note that, if not specifically mentioned, we use the testing dataset collected by our UAV-based system in lab environments for the following experiments by default.

6.4.2 Impact of the UAV's Uncontrollable Motion. To validate the effectiveness of our proposed distorted data filtering algorithm introduced in Section 4.2, we compare SoilIdNet's estimation accuracy on the original testing datasets with those on the testing data processed by the distorted data filtering (DDF) algorithm proposed in

Fig. 17. Light coverage on soil surface.

Fig. 18. Heavy coverage on soil surface.

Fig. 19. Reflectors of different materials in our tests.

Section 4.2. In Figure 16, we show the MAEs of SoilIdNet on the testing datasets of loamy soil, sand, and clay soil. We notice that the MAE is decreased by 1.61%, 2.14%, and 0.9% on loamy soil, sand, and clay soil respectively, if we filter the testing data using our distorted data filtering algorithm. Such results validate that our distorted data filtering algorithm that discards the data contaminated by the UAV's uncontrollable motion enhances the moisture estimation accuracy.

6.4.3 Impact of the Multipath Interference. To evaluate the impact of the multipath interference on the soil moisture estimation, we conduct experiments on loamy soil, sand, and clay soil in an outdoor garden with plenty of bushes and trees which provide rich multipath reflections. Specifically, in order to exclude the effect of the uncontrollable factor of the UAV's motion in this set of experiments, we use the bracket-based system to collect the testing data. Furthermore, to mimic the raising process of the UAV, we manually raise the altitude of the IR-UWB radar such that its distance to the soil surface changes from 1m to 3m in a 20cm increment.

In Figure 20, we compare the MAE of SoilIdNet on the original testing data with that on the testing data processed by the multipath interference elimination (MIE) algorithm proposed in Section 4.3. We notice that the MAE is decreased by 1.1%, 1.86%, and 1.32% on loamy soil, sand, and clay soil respectively, if we filter the testing data using our multipath interference elimination algorithm. Such results validate that our multipath interference elimination algorithm that discards the data contaminated by multipath interference also helps enhance the moisture estimation accuracy.

6.4.4 Impact of the Soil Surface Coverage. In wild fields, there could be objects, such as leaves and stones, covering on the measurement points, which might distort the radar signals and thus influence the soil moisture measurement accuracy. To investigate the feasibility of SoilId in such scenario, we conduct experiments where soil surface coverage exists. The coverage settings are illustrated in Figure 17 and Figure 18, including the light coverage and heavy coverage. In the light coverage setting, there exist a few leaves and stones covering part of the soil surface. In the heavy coverage setting, plenty of grass, leaves, and stones cover the entire soil surface and the thickness of coverage is around 5cm. We conduct the coverage experiments on on loamy soil, sand, and clay soil, whose results are shown in Figure 21. From this figure, we could observe that the soil surface coverage indeed influences the accuracy of soil moisture estimation. Specifically, heavy coverage decreases the estimation accuracy more significantly than light coverage. However, even in the heavy coverage setting, the maximum MAE of SoilIdNet is just 0.54%. Thus, SoilIdNet can get satisfactory performance even if there are coverages on the measurement point.

6.4.5 Impact of the Reflector's Material. Due to the the stringent FCC power limit for UWB systems, which is -41.3 dBm/MHz, the reflector buried under the soil surface should be highly reflective and able to provide strong reflections for radar signals. Besides, the material of the reflector should be stable in the soil so that we can bury the reflector in the soil for years without replacement. We have tested four reflectors composed

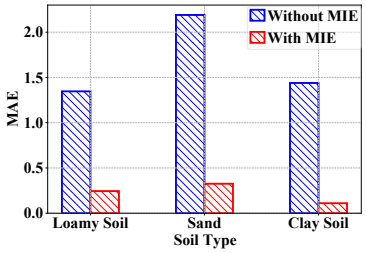

Fig. 20. MAEs of SoilIdNet with or without multipath interference elimination.

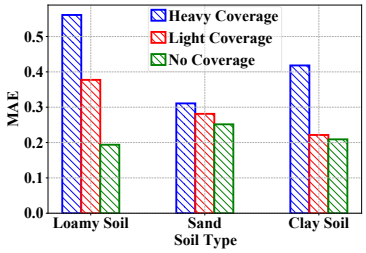

Fig. 21. MAEs of SoilIdNet under different levels of coverage.

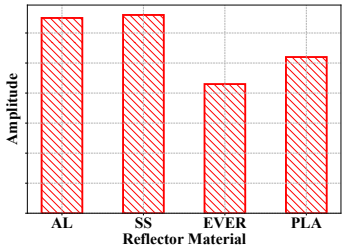

Fig. 22. Amplitude of $r_2(t)$ with reflectors composed of different materials.

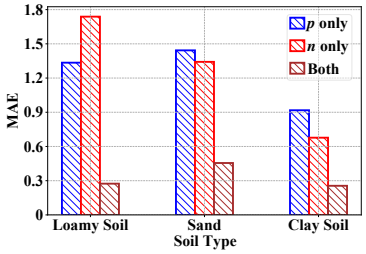

Fig. 23. MAEs of SoilIdNet with different input features.

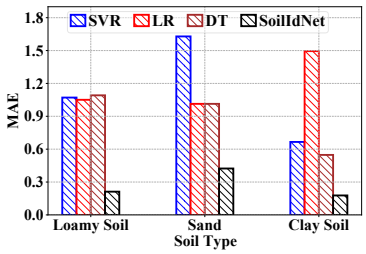

Fig. 24. MAEs of different machine learning methods.

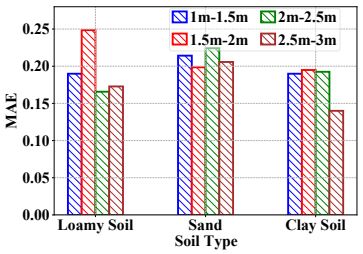

Fig. 25. MAEs for SoilIdNet under different soil surface-radar distance.

of different materials, i.e., aluminum (AL), stainless steal (SS), EVER, and plastic (PLA), as shown in Figure 19. The reflectors are buried 30cm below the soil surface. We plot the peak amplitude of $r_2(t)$ corresponding to the four reflectors in Figure 22. From this figure, we notice that the aluminum and stainless steal reflectors provide stronger reflections. In our experiments, we choose to use the aluminum plate, since it is cheaper than stainless steel, which is beneficial for potential wide area deployment. Besides, the dense oxide film that exists on the surface of the aluminum plate makes it resistive to the erosion by chemicals in the soil[8].

6.4.6 Impact of the Input Features. As described in Section 5.1, SoilIdNet takes both the soil RI and RAR as the input features to estimate the soil moisture. To validate that both of the features are useful for SoilIdNet to acquire accurate moisture estimation, we build two variants of SoilIdNet that only takes either soil RI or RAR as the input features for comparison. These two models share the same structure as the original SoilIdNet except that they only consist of one encoder module followed by an inference module. In Figure 23, we show the MAEs of the trained models with different features as inputs. From this figure, we notice that our SoilIdNet using both the soil RI and RAR as inputs has a lower MAE than the other two models on all the tested soil types. Such experimental results validate our design choice to take both the soil RI and RAR as input features, as they carry different soil moisture related information that helps SoilIdNet make accurate estimation.

6.4.7 Comparison of Different Machine Learning Methods. To validate our design of using the deep neural network model, i.e., SoilIdNet, to map the relationship between extracted radar signal features to soil moistures, we train other three machine learning models, i.e., support vector regression (SVR), linear regression (LR), decision tree (DT), and compare their performances with SoilIdNet. As shown in Figure 24, SoilIdNet outperforms the other three models on the testing datasets of loamy soil, sand, and clay soil. Such results indicate that employing the deep neural network structure, SoilIdNet has a more powerful representation ability than the other three machine learning models.

[8]The oxide film of aluminum is stable for years in the pH range of 4.5 to 8.5 [29], and the pH range of most types of soil is 5 to 8.5 [30].

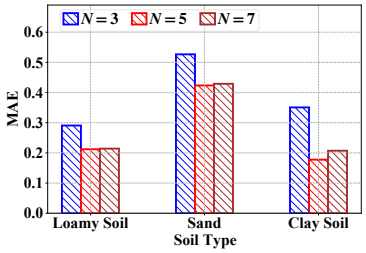

Fig. 26. MAEs for SoilIdNet with different N values.

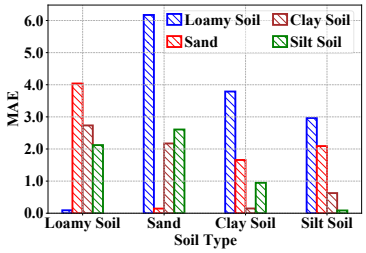

Fig. 27. MAEs for applying SoilIdNet trained on one type of soil to all soil types.

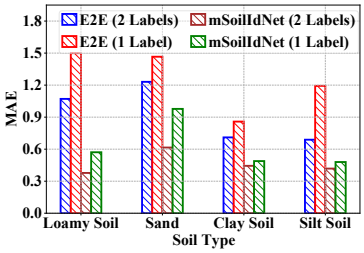

Fig. 28. Adaptation ability of models.

6.4.8 Impact of the Soil Surface-Radar Distance. To investigate how the soil surface-radar distance influence the accuracy of SoilIdNet, we divide the testing datasets into four groups, which are collected under the soil surface-radar distance of 1m-1.5m, 1.5m-2m, 2m-2.5m, and 2.5m-3m, respectively. In Figure 25, we show the MAEs of SoilIdNets on the testing datasets of loamy soil, sand, and clay soil. The MAEs are below 0.25% for all the experiments, whereas the MAEs do not show a clear correlation with soil surface-radar distance, which confirms with our intuition since the values of RARs and soil RIs are independent of the soil surface-radar distance, as introduced in Section 2.3. The experimental results indicate that the sensing accuracy of SoilIdNet is robust to the soil surface-radar distance, even if the soil surface-radar distance becomes as far as 3m.

6.4.9 Impact of Hyperparameters of SoilIdNet. To investigate how the hyperfarameters influence the performance of SoilIdNet, we implement variants of SoilIdNet with different encoder modules. Suppose N is the number of alternating FC layers and ReLU layers in the encoder modules. We implement three SoilIdNet with $N = 3$, $N = 5$, and $N = 7$, respectively. In Figure 26, we show the MAEs of the SoilIdNets on the testing datasets of loamy soil, sand, and clay soil. The SoilIdNet with $N = 5$ slightly outperforms the others on the testing datasets of each soil type. Thus, we choose $N = 5$ for SoilIdNet in all the experiments.

6.5 Performance of Fine-Tuned mSoilIdNet

6.5.1 Impact of the Soil Type. To validate that the SoilIdNet trained on one soil type may not generalize well to others, we first obtain four SoilIdNet models trained on datasets collected on individual four types of soil, respectively. Next, we apply each of the four models to estimate the moisture of all four types of soil, and obtain the estimation results shown in Figure 27. From this figure, we observe that SoilIdNet only obtains low MAE, when it is tested on the same type of soil in the training process. In contrast, on other types of soil, the performance of SoilIdNet is rather unsatisfactory.

6.5.2 Effectiveness of the mSoilIdNet Adaptation. We conduct several experiments to validate the effectiveness of our meta training and adaptation method proposed in Section 5.2. Specifically, we compare the adaptation ability of the pretrained mSoilIdNet model and an end-to-end (E2E) model. The E2E model is not pretrained and just adjusts its paramters from randomly initialized ones. We also prepare two groups of adaptation datasets for the target soil type. The first group consists of the data instances with only one kind of moisture label, whereas in the second group the data instances have two kinds of moisture labels. We adapt the pretrained mSoilIdNet and E2E model on these two groups of data respectively, and test the adapted models on the testing datasets. The results are shown in Figure 28. From this figure, we could observe that the MAE of the fine-tuned mSoilIdNet is much lower than that of the fine-tuned E2E model. Besides, we observe that the models adapted on the datasets with two moisture labels have better performance than those with only one moisture label. Such result is reasonable since more labels bring more useful information for fine-tuning the model. Furthermore, the average MAE of the fine-tuned mSoilIdNet is comparable to that yielded by training SoilIdNet with full labels of one type of soil, and

Fig. 29. (a) M3. (b) M4. (c) M5. (d) Aluminum reflector at M3.

Fig. 30. Radar signal collection and soil moisture measurement at M3 by the UAV-based system.

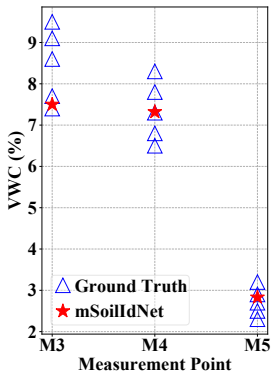

Fig. 31. Ground truth and estimated soil moisture of mSoilIdNet in field tests.

testing the trained SoilIdNet on the same soil type, as shown by Figures 27 and 28. Specifically, the former is only larger than the latter for 0.07%, which indicates the effectiveness of the fine-tuned mSoilIdNet.

6.6 Field Test

To evaluate the performance of our SoilId system in wild fields, we conduct field tests at three measurement points (M3, M4, and M5) on a lawn. As illustrated in Figure 29, we bury a 30cm × 30cm aluminum plate in the soil as the reflctor of each measurement point. Since the soil type in the field test is *a priori* unknown, we first collect the training data of at M3 using the bracket-based system for meta adaptation. After that, we collect the testing data of all the three measurement points using the UAV-based system for evaluation, as illustrated in Figure 30. The UAV is hovering over each measurement point to sense the soil moisture. The distance from the IR-UWB radar to the soil surface changes from 1m to 3m in a 20cm increment. Moreover, in real field tests, we cannot accurately control the soil moisture to be uniform at each measurement point as we do in lab environments. Thus, we manually collect five soil samples at each measurement point, and use the mean value of the ground truth moisture of the samples at M3 as the label of the dataset for meta adaptation. The meta model is pretrained with all the training dataset collected in the lab environments. As illustrated in Figure 31, the soil moisture estimation results of mSoilIdNet accurately fall in the range of the five ground truth moistures of the soil samples collected at each measurement point. The MAEs between the averages of the ground truth values at each measurement point and the estimated soil moistures are 0.76%, 0.1%, and 0.17% for M3, M4, and M5, respectively. The experimental results validate the effectiveness of the meta adaptation mechanism, which enables mSoilIdNet to achieve MAEs of lower than 0.8% in real-world field tests for all the three measurement points.

7 RELATED WORK

As discussed in Section 1, existing work on soil moisure sensing can be broadly categorized as sensor-based and RF-based techniques. Sensor-based techniques bury the dedicated sensor nodes in the soil to sense soil moistures. Several types of sensors have been proposed to measure an appropriate kind of soil property that is sensitive to moisture. For example, electricity resistance sensors [6] estimate moisture by measuring the electricity resistance between the two electrodes, and there also exist other types of soil moisture sensors such as capacitive sensors [31] heat-diffusion sensors [32], tensiometers sensors [8], and radioactive sensors [9] operating by different principles. The tedious labor work for installing the sensors and changing their batteries prevent these sensors

Table 1. Comparison with recent RF-based soil moisture sensing methods, where the sensing range refers to the distance between the soil surface and the above-ground device (e.g., radar board, antenna arrays) utilized by each method.

Method	RF Type	Avg. Error	Sensing Range	In-Soil Battery	UAV Test
CoMEt [18]	SDR	1.1%	0.6m	no	no
SoilTAG [40]	Wi-Fi	2%	6m	no	no
Tag+Radar [13]	IR-UWB radar	1.4%	4m	yes	no
GreenTag [36]	RFID	5%	2m	no	no
Strobe [10]	Wi-Fi	10%	1.5m	yes	no
Lora+Switch [12]	LoRa	3.1%	>5m	yes	no
smol [11]	LoRa	1.63%	1.95m	yes	no
SoilId	**IR-UWB radar**	**0.2%**	**3m**	**no**	**yes**

from the widespread usages. Besides, these sensors are either prohibitively expensive or inaccurate to yield fine-grained soil moisture estimations.

RF-based techniques do not require to deploy any sensor node, but some of them [10–13] also bury battery-powered devices in the soil. Specifically, Strobe [10] employs the propagation time and amplitude of Wi-Fi signals received by different antennas in the soil to jointly estimate soil moisture and salinity; The authors in [11, 12] propose to bury LoRa nodes in the soil to estimate the soil moisture based on the RSSI or the phase of LoRa signals; [13] proposes to bury a battery-powered tag in the soil and estimate the soil moisture based on the ToF from the tag to the radar. Other approaches [33, 34] also propose to bury a pair of UWB chips in the soil to estimate the soil moisture. However, the risk of soil contamination from battery corruption and the extra labor to replace the batteries limit the usage of these techniques.

Apart from these works, there are also other RF-based techniques that bury battery-free tags to provide reflections [35–37] of RF-signals, or just use the reflection of the soil surface and the boundaries between different soil layers for soil moisture sensing [14, 15, 18, 38, 39]. GreenTag [36] senses the moisture of the potted soil by utilizing the RFID tag attached to the exterior of the pot. However, its operation mode limits its application for in-ground soil moisture sensing in agricultural, and other wide-area soil moisture sensing scenarios. SoilTag [40] employs the Wi-Fi tag for soil moisture sensing. However, its accuracy is lower than that of SoilId, and SoilTag is not tested on UAV for mobile soil moisture sensing. [14–17, 38, 39] estimate the soil moisture through measuring soil surface reflections of the RF signals from spaceborne GNSS or radars carried on planes. These techniques can widely estimate soil moisture all over the earth, but could only operate at limited spatial resolutions. Apart from the remote sensing techniques, CoMEt [18] utilizes the signals reflected by the soil surface, as well as those by the boundaries of different soil layers to estimate the soil moisture. However, due to the limited power of the reflected signal strength, the operation range of CoMEt is within 60cm of the soil surface, which restricts its potential to be carried on aerial mobile platforms (e.g., UAVs) for wide-area soil moisture sensing.

Compared with these approaches, SoilId can quickly measure the soil moisture of multiple measurement points in a wide area, and can also provide moisture estimation with satisfactory spatial resolution and precision for agriculture, as well as other applications. We also comprehensively compare SoilId with the aforementioned recent RF-based soil moisture sensing methods in terms of sensing accuracy, the requirement of burying batteries in the soil, sensing range, and several other aspects in Table 1. As shown by this table, SoilId is the method with a lower error, and is the only work that performs system implementation on an actual UAV for soil moisture sensing compared with other recent RF-based soil moisture sensing methods [10–13, 18, 36, 40] listed in this table.

Apart from soil moisture sensing, the low cost and highly compact commercial miniature on-chip radars have shown rising popularity among lots of other sensing applications, such as through fog imaging and indoor

mapping [41–43], material sensing [44, 45], motion recognition and mesh recovery [46–49], as well as localization and bounding box estimation [50, 51], and many others [52–55]. Our work distinguishes from the above works [41–55] as we attach a miniature on-chip IR-UWB radar on an UAV and leverage it for a completely different task of soil moisture sensing.

8 CONCLUSION AND DISCUSSION

8.1 Conclusion

In this paper, we present SoilId, an RF-based soil moisture sensing system that combines a UAV and an IR-UWB radar to quickly perform wide-area soil moisture sensing without burying any in-ground battery-powered devices. To measure soil moisture, SoilId extracts soil moisture related features from the received radar signals, automatically detects and discards the data influenced by the UAV's uncontrollable motion and the multipath interference, and finally accurately maps the radar signal features to the soil moisture estimation through a novel deep neural network model SoilIdNet. Furthermore, we also augment the meta learning framework to obtain a meta model mSoilIdNet, which can be quickly fine-tuned on new target soil type with only a small number of labeled data. SoilId achieves a 50% quantile MAE of 0.23% on UAV tests. Besides, the meta model mSoilIdNet also shows its satisfactory adaptation ability in our extensive experiments.

8.2 Potential for Real-World Applications

8.2.1 Soil Moisture Sensing for a Large Area with SoilId. Clearly, a smart and automatic soil moisture monitoring system will release much human labor of carrying the sensing devices in a large sensing area. The highly mobile nature of SoilId makes the automatic soil moisture sensing in a large area possible. Users can program on the software development kit (SDK) to predefine the UAV's flight paths, and utilize the RTK modules or the visual markers to accurately localize the UAV. The soil surface-UAV distance can be accurately sensed by UAV's altitude sensing system [28] and automatically controlled through SDK. After that, the UAV can make soil moisture estimations at different measurement points consecutively in a fully automatic manner. The average time spent for measuring the soil moisture at a measurement point in our experiments is less than 2 minutes. Thus, SoilId supports fast measurement of the soil moistures at many measurement points in a wide area.

8.2.2 Low Cost Compared with Existing Systems. Existing large scale soil moisture sensing systems usually require to bury tens or even hundreds of sensors to provide enough coverage [56]. The high costs of reliable soil moisture sensor nodes ($100-$400 [7] each) make such systems prohibitively expensive. Compared with these systems, SoilId buries at each measurement point a battery-free aluminum reflector with attractive price ($5 each), which is 20× cheaper than the dedicated sensors. Meanwhile, SoilId does not require more efforts to deploy the reflectors, because the deployment density of the reflectors in SoilId is comparable to that of the sensors in existing systems. However, a soil moisture sensing system with sensors also requires to install various types of peripherals, such as sensor data loggers (more than $1000 each [7]) for data gathering and LoRa gateways for communications. These devices also bring extra costs and labor works to install and connect. SoilId does not require these peripherals because it can directly sense the soil moisture at each measurement point and store the results on the computing device on the UAV. The aluminum reflectors are chemically stable in soil for years without any maintenance. The major cost of SoilId comes from the UAV. However, nowadays many farms have already equipped with UAVs for other purposes (e.g., monitoring the growth of crops, spraying fertilizers and pesticides). The SoilId framework can be easily implemented on such UAV by integrating a Raspberry Pi and a commercial IR-UWB radar on it. The extra operation costs for soil moisture sensing are just the charging costs for extra flights. Thus, from the perspective of price, SoilId is also suitable for soil moisture sensing in large areas with multiple measurement points.

8.3 Limitations and Future Works

SoilId takes the first step to implement a UAV-based soil moisture sensing system with commercial IR-UWB radar and deep learning techniques, making it possible for modern smart agriculture to accurately monitor the soil moisture of a large sensing area. However, the potential of SoilId has not been fully exploited. We elaborate on the limitations and potential improvement directions for SoilId as follows.

8.3.1 Smaller Reflectors. In our experiments, we choose the reflector's size to be 30cm × 30cm, such that the UAV can easily align with the measurement point. However, it is far from the smallest size we can use. Smaller reflectors will reduce the deployment cost, and have less impact on the plant growth. Meanwhile, it is more difficult for the UAV to vertically align with the measurement point if we use smaller reflectors. Various choices of reflector size can be decided by considering the trade-off between environment friendliness and sensing convenience.

8.3.2 Other Choices of Radars with Different Operation Frequencies. SoilId employs the COTS IR-UWB radar whose central operation frequency is 7.29GHz to sense the soil moisture. Although the signals of such IR-UWB radar show satisfactory soil penetrating ability compared with other miniature on-chip radars radars, the performance of SoilId might be improved, if it is equipped with radars operating at lower frequencies. Since RF signal attenuates more slowly when its frequency is lower, if SoilId uses a radar with a lower operation frequency, it might sense deeper in the soil. Thus, in such case, the strengths of the signals reflected by the reflector will be higher, which will help promote the soil moisture sensing accuracy.

8.3.3 Effect of Plant Roots. Clearly, plant roots may change composition of the soil at the measurement points and further impact the soil moisture sensing accuracy. Luckily, such impact can be alleviated by manually removing the plant roots in advance when we construct a measurement point. However, it is possible that years after there might be new plant roots spread into the measurement point. We will leave the exploration of such impact on soil moisture sensing accuracy in our future work.

ACKNOWLEDGMENTS

This work was supported by NSF China (No. U20A20181, U21A20519) and supported by Alibaba Innovative Research (AIR) program.

REFERENCES

[1] U. S. E. P. Agency, "Watersense notice of intent (noi) to develop a draft specification for soil moisture-based control technologies," 2013.
[2] D. M. D, "Two decades of smart irrigation controllers in us landscape irrigation," vol. 63, no. 5, 2020, pp. 1593–1601.
[3] A. Tal, "Rethinking the sustainability of israel's irrigation practices in the drylands," *Water Research*, vol. 90, pp. 387–394, 2016.
[4] B. Garcia, "How to build a soil moisture monitoring system (tutorial)," https://blog.temboo.com/how-to-build-a-soil-moisture-monitoring-system/.
[5] P. V. Mauri, L. Parra, D. Mostaza-Colado, L. Garcia, J. Lloret, and J. F. Marin, "The combined use of remote sensing and wireless sensor network to estimate soil moisture in golf course," *Applied Sciences*, vol. 11, no. 24, p. 11769, 2021.
[6] H. Tian, Y. Shu, X.-F. Wang, M. A. Mohammad, Z. Bie, Q.-Y. Xie, C. Li, W.-T. Mi, Y. Yang, and T.-L. Ren, "A graphene-based resistive pressure sensor with record-high sensitivity in a wide pressure range," *Scientific reports*, vol. 5, no. 1, pp. 1–6, 2015.
[7] "Soil moisture sensors for irrigation scheduling," https://extension.umn.edu/irrigation/soil-moisture-sensors-irrigation-scheduling#electrical-resistance-sensors-1870361.
[8] E. Scientific, "Teros 21," https://edaphic.com.au/products/soils/mps-6-soil-water-potential-sensor/.
[9] I. Radiation Detection Technologies, "Radioactive Sensor."
[10] J. Ding and R. Chandra, "Towards low cost soil sensing using wi-fi," in *The Annual International Conference on Mobile Computing and Networking (Mobicom)*, 2019.
[11] D. Kiv, G. Allabadi, B. Kaplan, and R. Kravets, "smol: Sensing soil moisture using lora," in *Proceedings of the 1st ACM Workshop on No Power and Low Power Internet-of-Things*, 2022.

[12] Z. Chang, F. Zhang, J. Xiong, J. Ma, B. Jin, and D. Zhang, "Sensor-free soil moisture sensing using lora signals," *Proc. ACM Interact. Mob. Wearable Ubiquitous Technol (IMWUT).*, vol. 6, no. 2, pp. 45:1–45:27, 2022.
[13] C. Josephson, M. Kotaru, K. Winstein, S. Katti, and R. Chandra, "Low-cost in-ground soil moisture sensing with radar backscatter tags," in *ACM SIGCAS Conference on Computing and Sustainable Societies (Compass)*, 2021.
[14] N. Sue, "Review and evaluation of remote sensing methods for soilmoisture estimation," 2011.
[15] N. Eni, G and E. Dara, "Passive microwave remote sensing of soil moisture," 1996.
[16] K. Wu, G. A. Rodriguez, M. Zajc, E. Jacquemin, M. Clément, A. De Coster, and S. Lambot, "A new drone-borne gpr for soil moisture mapping," *Remote Sensing of Environment*, vol. 235, p. 111456, 2019.
[17] F. Abushakra, N. Jeong, D. N. Elluru, A. K. Awasthi, S. Kolpuke, T. Luong, O. Reyhanigalangashi, D. Taylor, and S. P. Gogineni, "A miniaturized ultra-wideband radar for uav remote sensing applications," *IEEE Microwave and Wireless Components Letters*, vol. 32, pp. 198–201, 2022.
[18] K. Usman, Mahmood and S. Muhammd, "Estimating soil moisture using rf signals," in *The Annual International Conference on Mobile Computing and Networking (Mobicom)*, 2022.
[19] A. Klotzsche, F. Jonard, M. C. Looms, J. van der Kruk, and J. A. Huisman, "Measuring soil water content with ground penetrating radar: A decade of progress," *Vadose Zone Journal*, vol. 17, no. 1, pp. 1–9, 2018.
[20] G. C. Topp, "Electromagnetic determination of soil water content: Measurements in coaxial transmission lines." vol. 16, no. 3, 1980, pp. 574–582.
[21] V. A. e. Rafael, "Moisture effects on the dielectric properties of soils," vol. 39, no. 1, 2001, pp. 125–128.
[22] L. Brocca, F. Melone, T. Moramarco, and R. Morbidelli, "Spatial-temporal variability of soil moisture and its estimation across scales," vol. 46, no. 2, 2010.
[23] J. Martínez-Fernández and A. Ceballos, "Mean soil moisture estimation using temporal stability analysis," vol. 312, no. 1-4, 2005, pp. 28–38.
[24] A. W. Western, R. B. Grayson, and G. Blöschl, "Scaling of soil moisture: A hydrologic perspective," vol. 30, no. 1, 2002, pp. 149–180.
[25] C. Finn, P. Abbeel, and S. Levine, "Model-agnostic meta-learning for fast adaptation of deep networks," in *Proceedings of the 34th International Conference on Machine Learning (ICML)*, 2017.
[26] K. Noborio, "Measurement of soil water content and electrical conductivity by time domain reflectometry: a review," vol. 31, no. 3, 2001, pp. 213–237.
[27] N. AS, "The world leader in ultra wideband (uwb) sensing," https://novelda.com/technology/.
[28] "Matrice 210 user manual," https://dl.djicdn.com/downloads/M200/20201120/M200_User_Manual_EN_20201120.pdf.
[29] B. Brown, "Corrosion resistance of aluminum," https://www.cmilc.com/resources/white-papers/corrosion-resistance-of-aluminum-pdf.
[30] "Soil quality indicators: ph," http://www.soilquality.org/indicators/soil_ph.html.
[31] Adrafruit, "Capacitive sensor," https://learn.adafruit.com/adafruit-stemma-soil-sensor-i2c-capacitive-moisture-sensor.
[32] P. C. Dias, W. Roque, E. C. Ferreira, and J. A. S. Dias, "A high sensitivity single-probe heat pulse soil moisture sensor based on a single npn junction transistor," *Computers and electronics in agriculture*, vol. 96, pp. 139–147, 2013.
[33] "Soil type characterization for moisture estimation using machine learning and uwb-time of flight measurements," *Measurement*, vol. 146, pp. 537–543, 2019.
[34] M. Malajner and D. Gleich, "Soil moisture estimation using uwb," in *2016 IEEE/ACES International Conference on Wireless Information Technology and Systems (ICWITS) and Applied Computational Electromagnetics (ACES)*, 2016.
[35] R. V. Aroca, A. C. Hernandes, D. V. Magalhães, M. Becker, C. M. P. Vaz, and A. G. Calbo, "Calibration of passive UHF RFID tags using neural networks to measure soil moisture," *Jding. Sensors*, vol. 2018, pp. 3 436 503:1–3 436 503:12, 2018.
[36] J. Wang, L. Chang, S. Aggarwal, O. Abari, and S. Keshav, "Soil moisture sensing with commodity rfid systems," in *Proceedings of the 18th International Conference on Mobile Systems, Applications, and Services (Mobisys)*, 2019.
[37] S. F. Pichorim, N. J. Gomes, and J. C. Batchelor, "Two solutions of soil moisture sensing with rfid for landslide monitoring," vol. 18, no. 2, 2018, pp. 452–563.
[38] S. H. Yueh, R. Shah, M. J. Chaubell, A. Hayashi, X. Xu, and A. Colliander, "A semiempirical modeling of soil moisture, vegetation, and surface roughness impact on cygnss reflectometry data," vol. 60, 2020, pp. 1–17.
[39] C. Chew and E. Small, "Soil moisture sensing using spaceborne gnss reflections: Comparison of cygnss reflectivity to smap soil moisture," vol. 45, no. 9, 2018, pp. 4049–4057.
[40] W. Jiao, J. Wang, Y. He, X. Xi, and X. Chen, "Detecting soil moisture levels using battery-free wi-fi tag," 2022.
[41] J. Guan, S. Madani, S. Jog, S. Gupta, and H. Hassanieh, "Through fog high-resolution imaging using millimeter wave radar," in *2020 IEEE/CVF Conference on Computer Vision and Pattern Recognition (CVPR)*, 2020.
[42] C. X. Lu, S. Rosa, P. Zhao, B. Wang, C. Chen, J. A. Stankovic, N. Trigoni, and A. Markham, "See through smoke: robust indoor mapping with low-cost mmwave radar," in *The 18th Annual International Conference on Mobile Systems (Mobisys)*, 2020, pp. 14–27.
[43] K. Qian, Z. He, and X. Zhang, "3d point cloud generation with millimeter-wave radar," *Proc. ACM Interact. Mob. Wearable Ubiquitous Technol (IMWUT).*, vol. 4, no. 4, pp. 148:1–148:23, 2020.

[44] Y. Liang, A. Zhou, H. Zhang, X. Wen, and H. Ma, "Fg-liquid: A contact-less fine-grained liquid identifier by pushing the limits of millimeter-wave sensing," *Proc. ACM Interact. Mob. Wearable Ubiquitous Technol (IMWUT).*, vol. 5, no. 3, pp. 116:1–116:27, 2021.
[45] C. Wu, F. Zhang, B. Wang, and K. J. R. Liu, "msense: Towards mobile material sensing with a single millimeter-wave radio," *Proc. ACM Interact. Mob. Wearable Ubiquitous Technol (IMWUT).*, vol. 4, no. 3, pp. 106:1–106:20, 2020.
[46] M. Zhao, Y. Liu, A. Raghu, H. Zhao, T. Li, A. Torralba, and D. Katabi, "Through-wall human mesh recovery using radio signals," in *2019 IEEE/CVF International Conference on Computer Vision (ICCV)*, 2019.
[47] C. X. Lu, M. R. U. Saputra, P. Zhao, Y. Almalioglu, P. P. B. de Gusmao, C. Chen, K. Sun, N. Trigoni, and A. Markham, "milliego: single-chip mmwave radar aided egomotion estimation via deep sensor fusion," in *The 18th ACM Conference on Embedded Networked Sensor Systems (Sensys)*, 2020.
[48] T. Liu, M. Gao, F. Lin, C. Wang, Z. Ba, J. Han, W. Xu, and K. Ren, "Wavoice: A noise-resistant multi-modal speech recognition system fusing mmwave and audio signals," in *The 19th ACM Conference on Embedded Networked Sensor Systems (Sensys)*, 2021.
[49] H. Xue, Q. Cao, H. H. Yan Ju, H. Wang, A. Zhang, and L. Su, "M4esh: mmwave-based 3d human mesh construction for multiple subjects," in *The 20th ACM Conference on Embedded Networked Sensor Systems (Sensys)*, 2022.
[50] E. Soltanaghaei, A. Prabhakara, A. Balanuta, M. G. Anderson, J. M. Rabaey, S. Kumar, and A. G. Rowe, "Millimetro: mmwave retro-reflective tags for accurate, long range localization," in *The 27th Annual International Conference on Mobile Computing and Networking (Mobicom)*, 2021.
[51] K. Bansal, K. Rungta, S. Zhu, and D. Bharadia, "Pointillism: accurate 3d bounding box estimation with multi-radars," in *The 18th ACM Conference on Embedded Networked Sensor Systems (Sensys)*, 2020.
[52] K. Cui, Q. Yang, L. Shen, Y. Zheng, and J. Han, "Integrated sensing and communication between daily devices and mmwave radars," in *The 20th ACM Conference on Embedded Networked Sensor Systems (Sensys)*, 2022.
[53] R. Ding, H. Jin, and D. Shen, "Rotation speed sensing with mmwave radar," in *The 42nd International IEEE Conference on Computer Communications (INFOCOM)*, 2023.
[54] Y. Feng, K. Zhang, C. Wang, L. Xie, J. Ning, and S. Chen, "mmeavesdropper: Signal augmentation-based directional eavesdropping with mmwave radar," in *The 42nd International IEEE Conference on Computer Communications (INFOCOM)*, 2023.
[55] L. Fan, L. Xie, X. Lu, Y. Li, C. Wang, and S. Lu, "mmmic: Multi-modal speech recognition based on mmwave radar," in *The 42nd International IEEE Conference on Computer Communications (INFOCOM)*, 2023.
[56] T. E. Ochsner, M. H. Cosh, R. H. Cuenca, W. A. Dorigo, C. S. Draper, Y. Hagimoto, Y. H. Kerr, K. M. Larson, E. G. Njoku, E. E. Small *et al.*, "State of the art in large-scale soil moisture monitoring," *Soil Science Society of America Journal*, vol. 77, no. 6, pp. 1888–1919, 2013.